Supplementary information

Sustainable Nanomanufacturing: Two-Dimensional Materials Transfer Using a Bioderived and Biodegradable Supportive Polymer.

*Md Arifur R. Khan[1], Swapna Kalkar[1], Besan Khader[1], Olubunmi O. Ayodele[1], *Aleksandrs Prokofjevs[2], *Tetyana Ignatova[1]*

[1]Department of Nanoscience, Joint School of Nanoscience and Nanoengineering, University of North Carolina at Greensboro, NC.

[2]Department of Chemistry, North Carolina Agricultural and Technical State University, NC.

From biomass to biodegradable polymer

Poly-angelica lactone (PAL) synthesized from levulinic acid, are considered an excellent potential substitute for currently used polymers (e.g., PMMA) in 2D materials transfer. Levulinic acid (LA) is an exceptionally valuable biobased compound capable of undergoing numerous chemical transformations, resulting in the generation of diverse and practical compounds with a wide range of applications [1]. Pharmaceuticals, flavors & perfumes, agrochemicals, food additives, personal care products, resins and coatings, plasticizers, solvents, fuel additives, and biofuels are just a few of the items that use LA as a precursor [2–7]. LA (a carboxylic acid) can be made from a variety of feedstocks, including industrial byproducts, biomass feedstocks like lignocellulosic materials, agricultural residues, and energy crops, sugars like glucose or fructose, and starch, a carbohydrate polymer found in crops like corn, wheat, and potatoes [8,9]. Dehydration of LA causes intramolecular condensation leading to the formation of α-angelica lactone (5-methyl-2(3H) furanone) [10,11] that can also be naturally found in agroproducts like soybean and grapes having enormous applications in varied fields including dairy products [12,13]. Representation of a synthesis route for producing α-angelica lactone (α-AL) from the industrial biomass has been shown in Figure S1, that can undergo biodegradable polymerization.

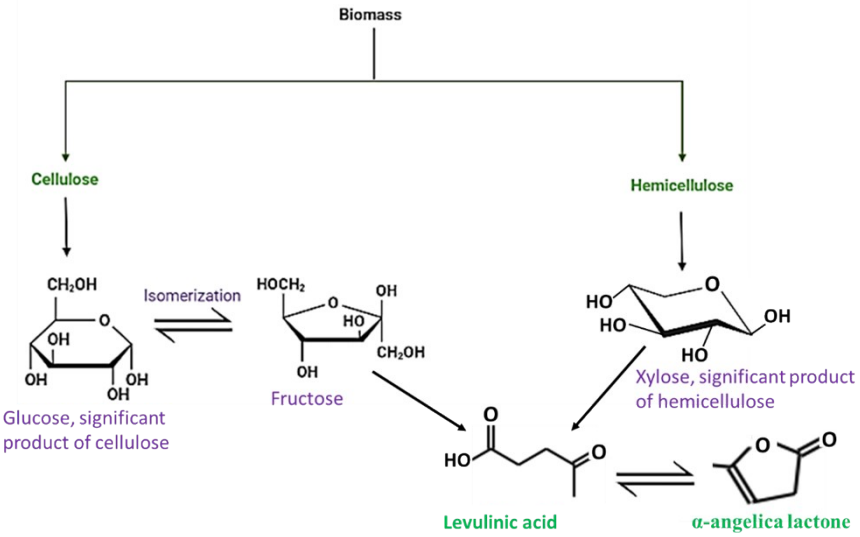

Figure S1: Production of angelica lactone from industrial biomass

FTIR of as synthesized PAL-14d

The FTIR spectrum of the as synthesized treated PAL-14d in Figure S2 resembled the polymer with a broad peak of the -OH group ranging from 3100 to 3600 cm^{-1}. Furthermore, due to the great number of repeating units, the peaks are prominent. By cleaning the polymer as described in the main paper, it was possible to obtain FTIR spectra that resembled the C-O and C=C bonds.

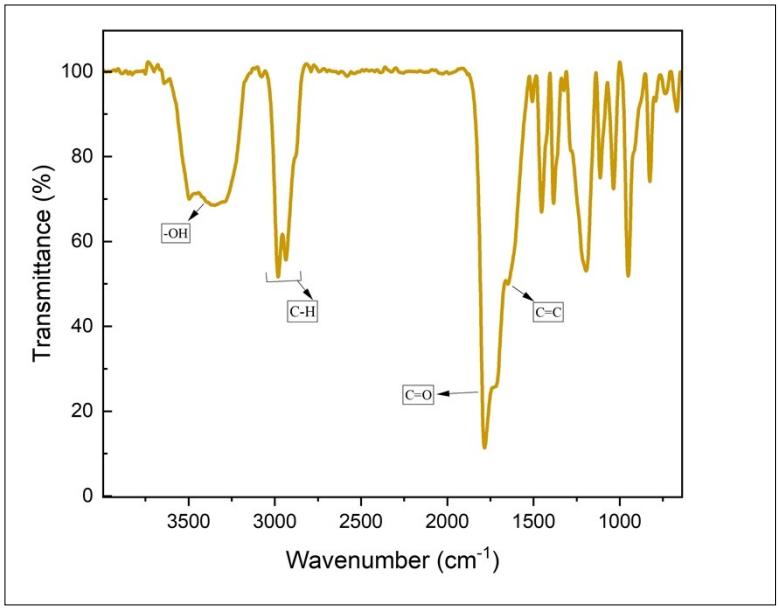

Figure S2: FTIR spectrum of purified PAL-14d.

^{1}H NMR of PAL-1d and PAL-1d purification supernatant in $CDCl_3$

The NMR analysis was done on precipitate formed during the thorough purification of the crude PAL-1d. The NMR spectrum of the purified PAL-1d further indicates ring-opening polymerization of AL, as shown in Figure S3, as it is consistent with the previously reported ^{1}H NMR of poly (a-angelica lactone) [9]. However, the peak of the hydroxyl group, COOH, which typically shows up around 12 ppm, is not present in the spectrum, even though the IR spectrum shows its stretching vibration (Figure 2b in main paper). In addition, the supernatant of the purification process was collected and characterized with NMR to ensure that the β-AL dimers are separated from the PAL-1d (Figure S4).

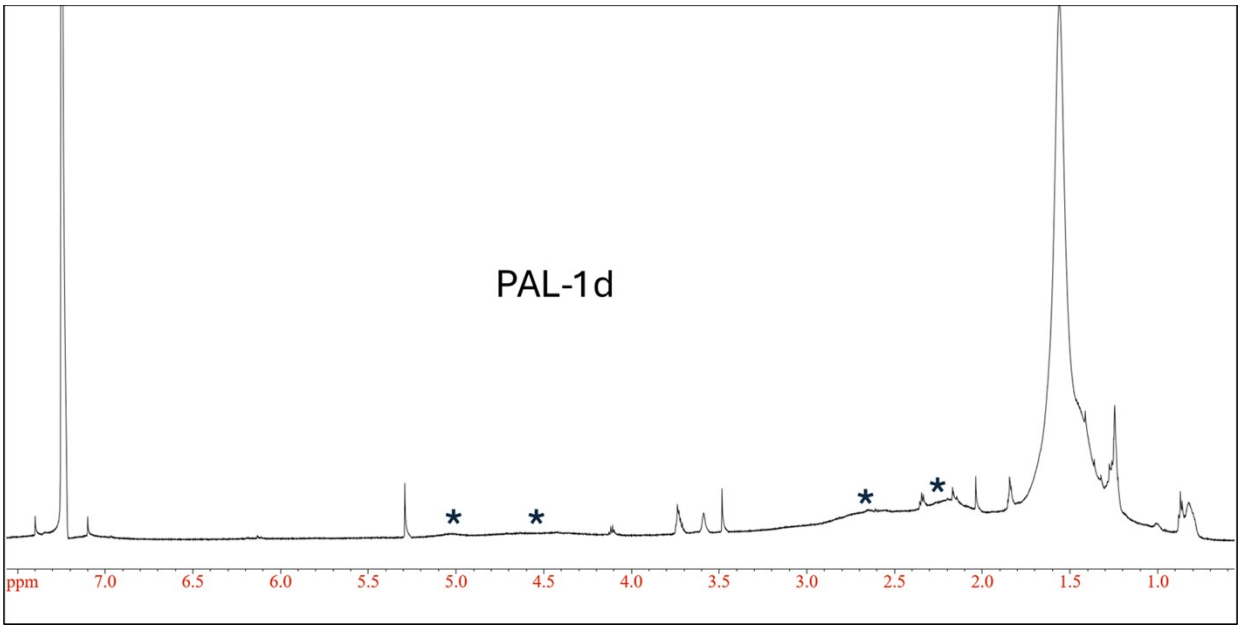

Figure S3: ^{1}H NMR of PAL-1d in $CDCl_3$. Three major peaks (labeled with *) relate to the protons of the purified polyester: δ1.2, 1.5, 5.3. These peaks imply ring-opening polymerization, except of the COOH peak that is not present (area not shown) due to the low concentration of the purified polyester in the NMR sample.

Since the treatment of the crude PAL-1d using ethyl acetate and hexanes resulted in the precipitation of the clean polyester, both the precipitate and supernatant were characterized via ^{1}H NMR ($CDCl_3$). The ^{1}H NMR spectrum of the supernatant (Figure S4) shows that the hexanes-soluble portion of the polyester, the supernatant, contains β-AL dimers, as observed in [14]. This implies that most of the precipitate is the α-AL polyester, as presented in the main paper.

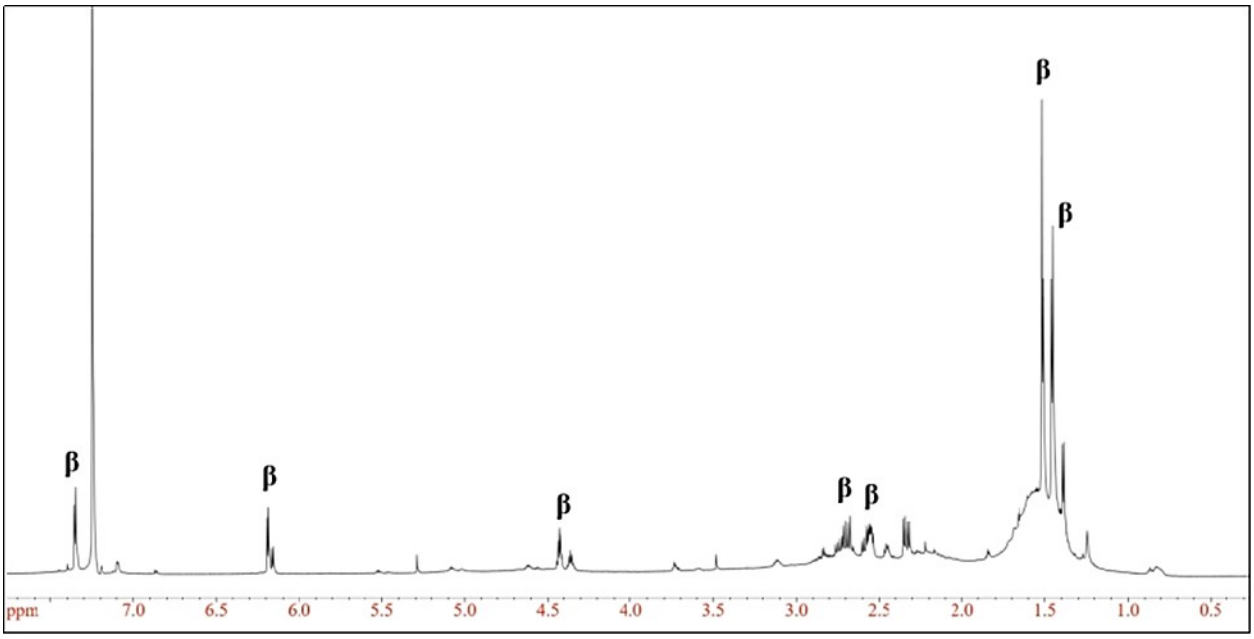

Figure S4: ^{1}H NMR of PAL-1d purification supernatant in $CDCl_3$

Graphene transfer by etching and bubbling method

Monolayer graphene was transferred following the protocol mentioned in main paper. As synthesized but unclean PAL-1d was coated on graphene/copper and transferred by etching method. SEM images of this sample has been shown in (Figure S5a, b) that confirms the compatibility of this polymer with both etching and bubbling method. Additionally, graphene was transferred using unpurified PAL-14d by bubbling method and corresponding SEM images are shown in (Figure S5c, d). Though the time required for removal of polymer was less than 25 minutes the residue of polymer is less. This implies that both, PAL-1d and PAL-14d, are compatible for several traditional transfer methods like etching and bubbling.

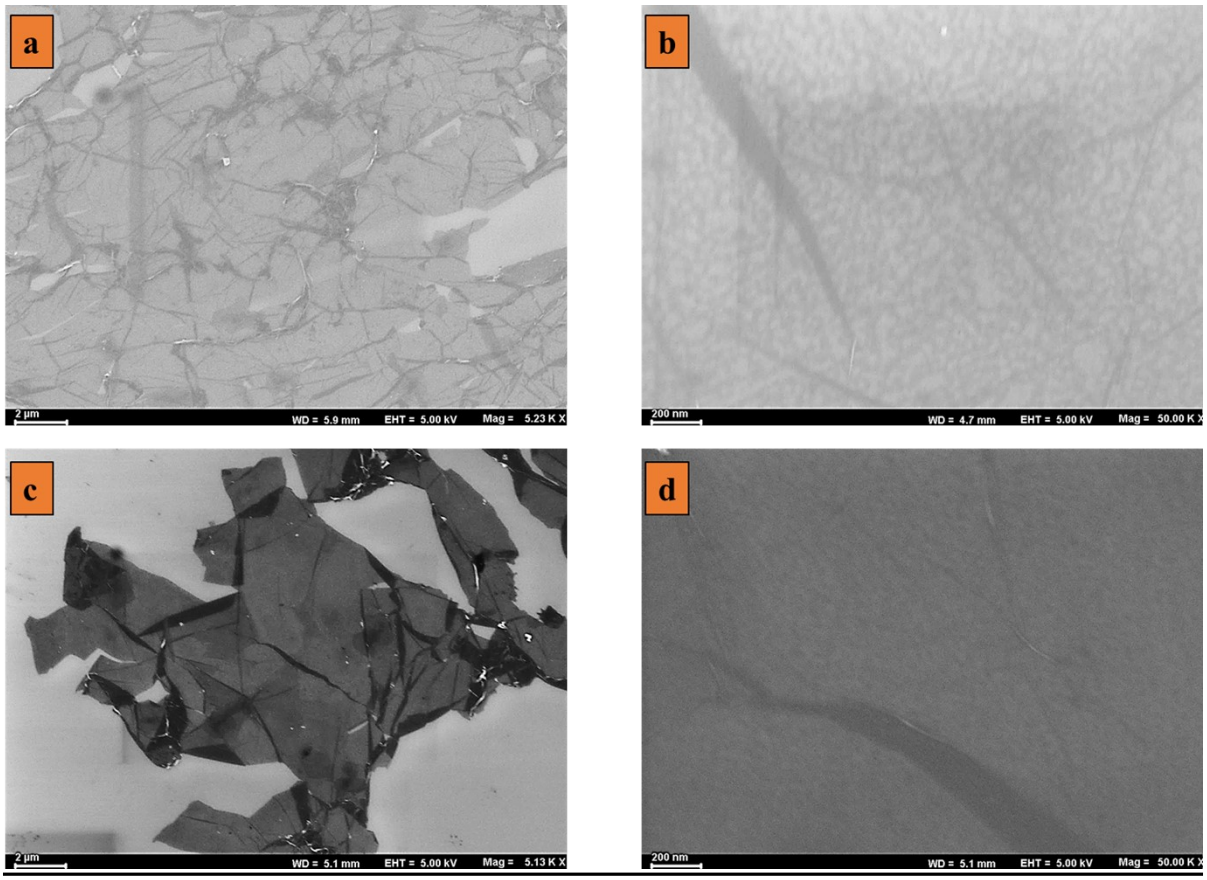

Figure S5: SEM images of graphene transferred using unclean PAL under different conditions: (a, b) PAL-1d via the etching method and (c, d) unclean PAL-14d via the bubbling method. (a, c) 5k magnification and (b, d) 50k magnification. Scale bars are 2 µm for (a, c) and 200 nm (b, d)

PAL biodegradation for yeast-assisted graphene transfer.

For biodegradability test, a small aliquot of yeast culture (product from ATCC) solid colonies added in 25ml liquid YPD medium prepared under laboratory conditions. Culture grown overnight in 250 mL Erlenmeyer flasks at 30°C with 100 rpm in shaking incubator then centrifuged it next day in falcon tube and removed supernatant, which is YPD medium, then washed with deionized water and separated aqueous suspension of pure microbial culture of ***S. cerevisiae***.

PAL-1d. Figure S6 shows the degradation of PAL-1d over time. For the first couple of days the change in the sample was not vivid to be visualized. However, careful observation of the sample from 10th day to 33rd day (Figure S6) revealed a progressive exposure of the substrate beneath the PAL layer over time. A possible explanation is that once an area was completely cleared of PAL, the yeast migrated to adjacent PAL regions, thereby accelerating the process.

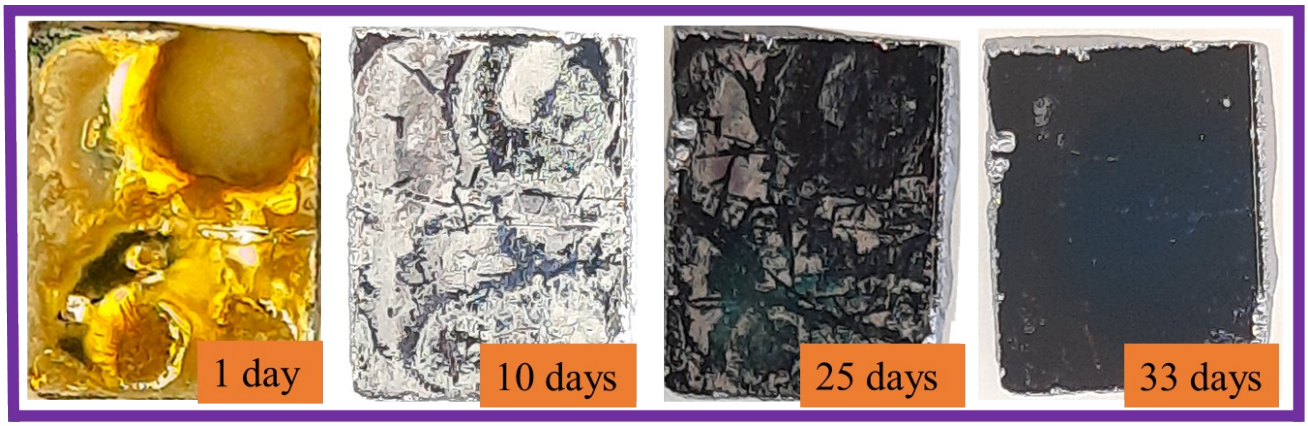

Figure S6: Gradual degradation of PAL-1d over 33 days.

PAL-14d. The PAL-14d coated graphene was transferred on SiO_2/Si substrate by bubbling method as mentioned in the main paper. After the transfer PAL-14d/graphene/ SiO_2/Si was treated with ***S. cerevicea*** for 11 days by incubating the sample into the *S. cerevicea solution* instead of removing the polymer by chemical treatment and then cleaned with only DI water. Optical microscope observation (Figure S7a, b) reveals that significant amount of PAL was removed by ***S. cerevicea*** while the remaining amount was due because of high coating thickness that require more time for complete degradation. Several areas of graphene were exposed after ***S. cerevicea*** treatment as shown in Figure S7c. Exposure of graphene after ***S. cerevicea*** treatment was confirmed by optical microscope observation, Raman spectroscopy and SEM images. Figure S7d represents the electron microscopic image of graphene exposed after biodegradation and Figure S7e represents the Raman spectrum of monolayer graphene. Additionally, heat map of graphene 2D Raman spectra intensity produced from 8µm x 8µm scanning area also confirmed the biodegradability of PAL-14d.

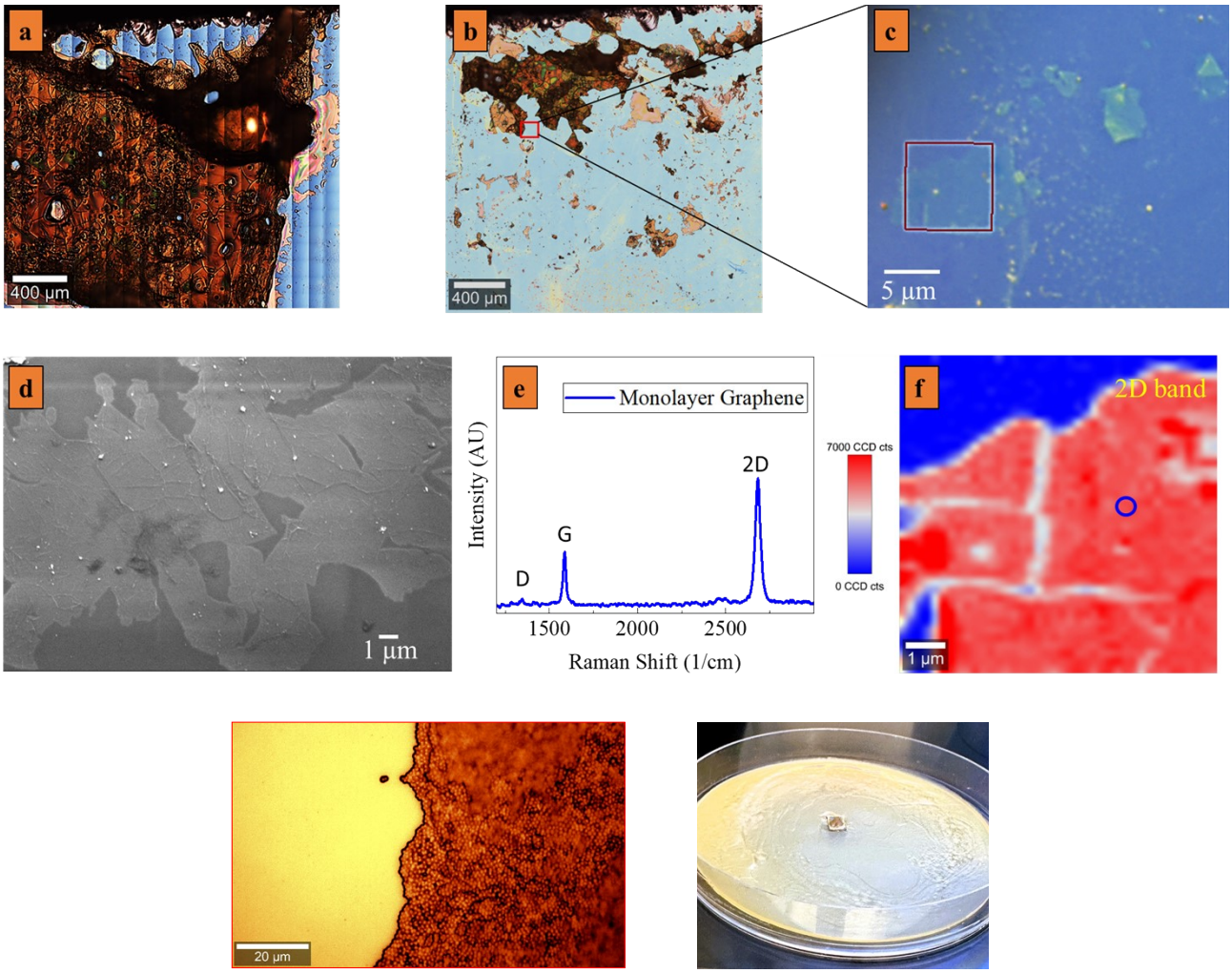

Figure S7: Optical images of PAL-14d/graphene/SiO_2/Si composite sample before (a) and after (b) degradation by ***S. cerevicea***. Exposed graphene areas observed at 10X magnification (c) and SEM image (d) of the exposed graphene region at 6k magnification after PAL-14d removed by ***S. cerevicea***. Raman spectrum confirming monolayer graphene (e) and heat map of 2D peak intensity (f) for 8µm x 8µm mapping area (corresponding to the red rectangular region in Fig. c). Bottom left: 100X magnification of red rectangular area in (b). Bottom right: incubation sample in the *S. cerevicea solution.*

Raman Correlation Analysis

The Raman frequencies of graphene, notably the G (ω_1) and 2D (ω_2) modes, exhibit remarkable sensitivity to both strain and doping effects on the monolayer graphene (MLG). These dependencies are mathematically described by the equations (1,2).

$$\Delta\omega_1 = -2\gamma_1\omega_1{}^0\varepsilon + k_1 n, \quad (1)$$

$$\Delta\omega_2 = -2\gamma_2\omega_2{}^0\varepsilon + k_2 n. \quad (2)$$

where γ is the Grüneisen parameter corresponding to the frequency of peak ω, and ω^0 is the frequency corresponding to zero strain/dope, n is the carrier concentration and K is a constant. Experimentally determined Grüneisen parameters for graphene are 1.9 and 2.6 for G (ω_1), 2D (ω_2) mode respectively. While subscript 1 and 2 represents the pair of peaks G-2D, the value of K_1 is -9.6×10^{-13} for G, and value of K_2 is -1×10^{-13} for 2D [15–21]. By solving the equations 1 and 2 we can calculate the amount of strain (ε) and doping (n) from the following rearranged equations (3,4).

$$\varepsilon = (k_1 \Delta\omega_2 - k_2 \Delta\omega_1) / (2\gamma_1\omega_1{}^0 k_2 - 2\gamma_2\omega_2{}^0 k_1) \quad (3)$$

$$n = (\gamma_1\omega_1{}^0 \Delta\omega_2 - \gamma_2\omega_2{}^0 \Delta\omega_1) / (\gamma_1\omega_1{}^0 k_2 - \gamma_2\omega_2{}^0 k_1) \quad (4)$$

Thus, by conducting correlation analysis of Raman frequencies (G vs 2D), valuable insights into the material's condition, including strain and doping levels, can be uncovered. Strain in MLG is found as a cluster of data along the 2.2 slope line (axis for uniaxial (hydrostatic) strain) as reported in [22–24]. The slope line for p doped MLG is 0.55 as reported by [25].

Summary of graphene transfer procedure steps

The detailed steps of the graphene transfer using PAL supportive polymer is presented below on Figure S8, where all possible routes are shown.

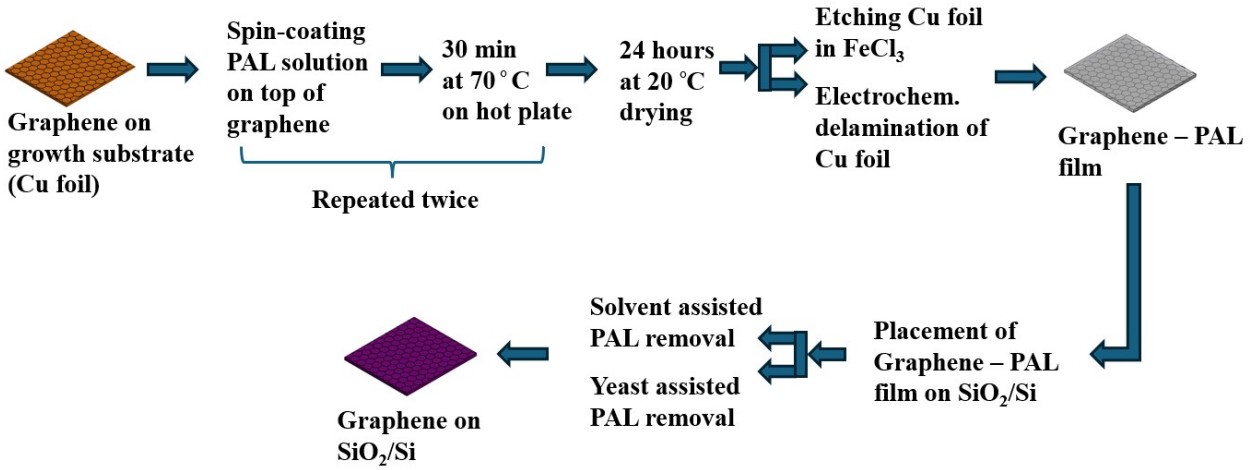

Figure S8: Schematic of CVD-grown graphene transfer from Cu foil to SiO_2/Si substrate.

Transfer and characterization of CVD grown MoS_2

The MoS_2 samples for this publication was provided by The Pennsylvania State University Two-Dimensional Crystal Consortium – Materials Innovation Platform (2DCC-MIP). The transfer of MoS2 from a sapphire substrate to a SiO_2/Si substrate was accomplished through a carefully orchestrated process that blends traditional techniques with precision. Initially, pristine metalorganic chemical vapor deposition (MOCVD) grown MoS_2 on a sapphire substrate was treated to a two-step spin coating process utilizing a solution comprising 75 wt% clean PAL-1d (poly angelica lactone) in acetone. The first spin coating cycle involved parameters of 400 rpm for 15 seconds, followed by a subsequent cycle at 500 rpm for 45 seconds. After the first coating, the sample underwent a crucial thermal treatment step, residing on a hot plate at 70 °C for 30 minutes. Following this, a second coating was applied, followed by a 24-hour period of natural drying at room temperature. To facilitate the detachment of the PAL-1d/MoS_2 composite from the sapphire substrate, thermal tape was meticulously applied to the structure. Subsequently, an 80-minute sonication process in water at 70 °C effectively delaminated the composite, leaving the tape/PAL/MoS_2 assembly ready for transfer to the desired substrate (SiO_2/Si). This assembly underwent further thermal treatment on a hot plate, this time at 150 °C, resulting in the controlled peeling off the thermal tape, while the PAL-1d/MoS_2 composite securely adhered to the target substrate. In the final step, the PAL-1d film was gently removed through a 30-minute sonication in an acetone bath, culminating in the successful fabrication of a MoS_2 device positioned atop a SiO_2/Si substrate.

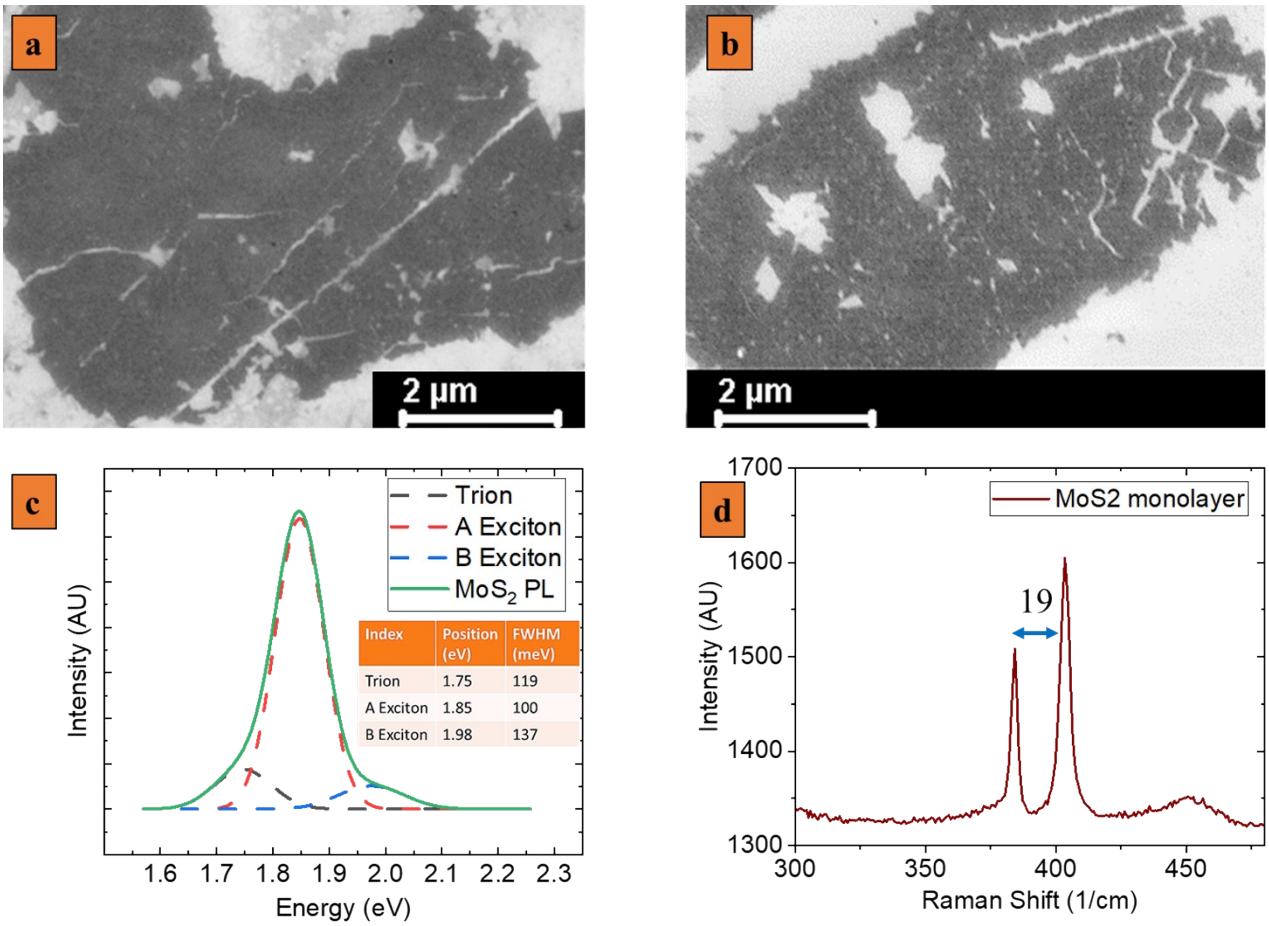

Figure S9: Morphological study and optical properties of PAL-1d assisted transfer of MOCVD grown monolayer MoS_2. SEM images (a, b), photoluminescence spectra (c) and Raman spectra (d).

We evaluated the quality of transferred MoS_2 by SEM imaging, Raman and photoluminescence spectroscopy (Figure S9a). SEM imaging revealed a few cracks and holes in the sample, which are attributed to handling. A key factor influencing the transfer quality is the coating of the polymer film over the samples. When the PAL solution concentration is too low, holes may form during drying, which can impact the quality of the transferred sample. Optimizing the balance between PAL solution concentration and spin-coating parameters through further refinement will enhance the transfer quality of TMDC samples.

The monolayer and few-layer MoS_2 crystals exhibit a direct bandgap nature, making photoluminescence characterization a profoundly enlightening tool for understanding their optical properties. Two photoluminescence (PL) peaks are observed in MoS_2 monolayer, a prominent A exciton peak between 1.8 and 1.9 eV and a B exciton peak around 2 eV. A negatively charged

exciton, known as a trion, typically appears at a lower energy than the A exciton PL peak due to electron doping in MoS_2 on silica substrate [21,26–28] (Fig. S9c). In monolayer MoS_2 at the K-point, energy splitting of valence band due to the spin-orbit interaction can be calculated by the energy difference of A and B exciton peaks. In this experiment we found the energy difference to be 130 meV that is in good agreement with previous study [26,29]. The FWHM of A exciton has been found to be 100 meV which is also comparable with the prior work [30,31].

Raman spectroscopy is widely used to understand the quality and to determine the number of layers in 2D crystals including MoS_2 [20,21,32,33]. Two prominent Raman peaks at around 383 cm^{-1} and 403 cm^{-1} are attributed to the E_{2g} (in plane) and A_{1g} (out of plane) phonon vibration modes respectively. The separation of these two vibrations is indicative of number layers. For single layer, difference between the vibrational modes is 19-20 cm^{-1}, while for double layer the difference is 21-22 cm^{-1}. Raman spectrum of this sample showed monolayer response having E_{2g} and A_{1g} modes at 384 cm^{-1} and 403 cm^{-1} respectively with a separation of 19 cm^{-1} (Figure S9d).

References:

1. Pileidis, F. D. & Titirici, M. M. Levulinic Acid Biorefineries: New Challenges for Efficient Utilization of Biomass. *ChemSusChem* **9**, 562–582 (2016).
2. Kitano, M., F, T. & M, O. Levulinic Acid, A New Chemical Raw Material. Its Chemistry and Use. *Levulinic Acid* (1975).
3. Thomas, J. J., and R. G. Barile. "Conversion of cellulose hydrolysis products to fuels and chemical feedstocks." *Biomass Wastes* **8**, 1461-1494 (1985).
4. Bozell, J. J. *et al.* Production of levulinic acid and use as a platform chemical for derived products. *Resour Conserv Recycl* **28**, 227–239 (2000).
5. Corma Canos, A., Iborra, S. & Velty, A. Chemical routes for the transformation of biomass into chemicals. *Chem Rev* **107**, 2411–2502 (2007).
6. Rackemann, D. W. & Doherty, W. O. The conversion of lignocellulosics to levulinic acid. *Biofuels, Bioproducts and Biorefining* **5**, 198–214 (2011).
7. Huber, G. W., Iborra, S. & Corma, A. Synthesis of transportation fuels from biomass: Chemistry, catalysts, and engineering. *Chem Rev* **106**, 4044–4098 (2006).

8. Antonetti, C., Licursi, D., Fulignati, S., Valentini, G. & Galletti, A. M. R. New Frontiers in the Catalytic Synthesis of Levulinic Acid: From Sugars to Raw and Waste Biomass as Starting Feedstock. *Catalysts 2016, Vol. 6, Page 196* **6**, 196 (2016).

9. Tarabanko, V. E. & Kaygorodov, K. L. *Chemistry for Sustainable Development 18 (2010) 321–328 New Biodedradable Polymers Based on α-Angelicalactone*.

10. Xin, J. *et al.* Formation of C-C bonds for the production of bio-alkanes under mild conditions. *Green Chemistry* **16**, 3589–3595 (2014).

11. Lima, C. G. S., Monteiro, J. L., de Melo Lima, T., Weber Paixão, M. & Corrêa, A. G. Angelica Lactones: From Biomass-Derived Platform Chemicals to Value-Added Products. *ChemSusChem* vol. 11 25–47 Preprint at https://doi.org/10.1002/cssc.201701469 (2018).

12. Lindström, M., Hedenström, E., Bouilly, S., Velonia, K. & Smonou, I. Synthesis of diastereo- and enantiomerically pure anti-3-methyl-1,4-pentanediol via lipase catalysed acylation. *Tetrahedron Asymmetry* **16**, 1355–1360 (2005).

13. Swift, K. A. D. Advances in Flavours and Fragrances From the Sensation to the Synthesis RSeC Royal Society of Chemistry.

14. Wang, X. J. & Hong, M. Lewis-Pair-Mediated Selective Dimerization and Polymerization of Lignocellulose-Based β-Angelica Lactone into Biofuel and Acrylic Bioplastic. *Angewandte Chemie International Edition* **59**, 2664–2668 (2020).

15. Proctor, J. E. *et al.* High-pressure Raman spectroscopy of graphene. *Phys Rev B Condens Matter Mater Phys* **80**, 073408 (2009).

16. Zabel, J. *et al.* Raman spectroscopy of graphene and bilayer under biaxial strain: Bubbles and balloons. *Nano Lett* **12**, 617–621 (2012).

17. Cheng, Y. C., Zhu, Z. Y., Huang, G. S. & Schwingenschlögl, U. Grüneisen parameter of the G mode of strained monolayer graphene. *Phys Rev B Condens Matter Mater Phys* **83**, 115449 (2011).

18. Mohiuddin, T. M. G. *et al.* Uniaxial strain in graphene by Raman spectroscopy: G peak splitting, Grüneisen parameters, and sample orientation. *Phys Rev B Condens Matter Mater Phys* **79**, 205433 (2009).

19. Lee, Y. R., Huang, J. X., Lin, J. C. & Lee, J. R. Study of the Substrate-Induced Strain of As-Grown Graphene on Cu(100) Using Temperature-Dependent Raman Spectroscopy: Estimating the Mode Grüneisen Parameter with Temperature. *Journal of Physical Chemistry C* **121**, 27427–27436 (2017).

20. Schmidt, K., Trofe, A. & Ignatova, T. Communication–Multimodal Image Correlation in Two-Dimensional Materials via Automated Image Processing by Strain and Doping Analysis. *ECS Journal of Solid State Science and Technology* **11**, 121007 (2022).

21. Ignatova, T. *et al.* Multidimensional Imaging Reveals Mechanisms Controlling Multimodal Label-Free Biosensing in Vertical 2DM-Heterostructures. *ACS Nano* **16**, 2598–2607 (2022).

22. Mueller, N. S. *et al.* Evaluating arbitrary strain configurations and doping in graphene with Raman spectroscopy. *2d Mater* **5**, (2018).

23. Lee, J. E., Ahn, G., Shim, J., Lee, Y. S. & Ryu, S. Optical separation of mechanical strain from charge doping in graphene. *Nat Commun* **3**, (2012).

24. Ayodele, O. O., Pourianejad, S., Trofe, A., Prokofjevs, A. & Ignatova, T. Application of Soxhlet Extractor for Ultra-clean Graphene Transfer. *ACS Omega* **7**, 7297–7303 (2022).

25. Froehlicher, G. & Berciaud, S. Raman spectroscopy of electrochemically gated graphene transistors: Geometrical capacitance, electron-phonon, electron-electron, and electron-defect scattering. *Phys Rev B Condens Matter Mater Phys* **91**, 205413 (2015).

26. Mak, K. F. *et al.* Tightly bound trions in monolayer MoS2. *Nature Materials 2012 12:3* **12**, 207–211 (2012).

27. Scheuschner, N. *et al.* Photoluminescence of freestanding single- and few-layer MoS 2. *Phys Rev B Condens Matter Mater Phys* **89**, 125406 (2014).

28. Lin, Y. C. *et al.* Recent Advances in 2D Material Theory, Synthesis, Properties, and Applications. *ACS Nano* vol. 17 9694–9747 Preprint at https://doi.org/10.1021/acsnano.2c12759 (2023).

29. Komider, K., González, J. W. & Fernández-Rossier, J. Large spin splitting in the conduction band of transition metal dichalcogenide monolayers. *Phys Rev B Condens Matter Mater Phys* **88**, 245436 (2013).

30. Lin, Y. *et al.* Dielectric screening of excitons and trions in single-layer MoS2. *Nano Lett* **14**, 5569–5576 (2014).

31. Sercombe, D. *et al.* Optical investigation of the natural electron doping in thin MoS 2 films deposited on dielectric substrates. *Sci Rep* **3**, (2013).

32. Lee, C. *et al.* Anomalous lattice vibrations of single- and few-layer MoS2. *ACS Nano* **4**, 2695–2700 (2010).

33. Aryeetey, F., Ignatova, T. & Aravamudhan, S. Quantification of defects engineered in single layer MoS 2. *RSC Adv* **10**, 22996–23001 (2020).